The global version of the gyrokinetic turbulence code GENE

T. Görler[a,*], X. Lapillonne[b], S. Brunner[b], T. Dannert[c], F. Jenko[a], F. Merz[a], D. Told[a]

[a]*Max-Planck-Institut für Plasmaphysik, EURATOM Association, D-85748 Garching, Germany*
[b]*École Polytechnique Fédérale de Lausanne, CRPP, CH-1015 Lausanne, Switzerland*
[c]*Rechenzentrum der Max-Planck-Gesellschaft, D-85748 Garching, Germany*

Abstract

The understanding and prediction of transport due to plasma microturbulence is a key open problem in modern plasma physics, and a Grand Challenge for fusion energy research. Ab initio simulations of such small-scale, low-frequency turbulence are to be based on the gyrokinetic equations, a set of nonlinear integro-differential equations in reduced (five-dimensional) phase space. In the present paper, the extension of the well-established and widely used gyrokinetic code GENE [F. Jenko *et al.*, Phys. Plasmas **7**, 1904 (2000)] from a radially local to a radially global (nonlocal) version is described. The necessary modifications of both the basic equations and the employed numerical methods are detailed, including, e.g., the change from spectral methods to finite difference and interpolation techniques in the radial direction and the implementation of sources and sinks. In addition, code verification studies and benchmarks are presented.

Keywords: Plasma turbulence, transport in plasmas, gyrokinetics, plasma simulation.
PACS: 52.35.Ra, 52.25.Fi, 52.30.Gz, 52.65.-y

1. Introduction

One of the key physics problems on the way to efficient fusion power plants based on toroidal magnetic confinement is the thorough understanding and reliable prediction of the so-called anomalous transport of heat, momentum, and particles across the magnetic surfaces (hereafter referred to as the radial direction). This effect, which significantly degrades the quality of the plasma confinement (thus preventing burning plasmas in present-day experiments), is commonly attributed to small-scale (roughly comparable to the ion or electron gyroradius), low-frequency (much smaller than the ion and electron gyrofrequency) turbulence driven by microinstabilities which extract free energy from the background temperature and density gradients.

Since the high-temperature, low-density fusion plasmas are only weakly collisional, kinetic theory provides the appropriate framework for their theoretical description. In principle, this would amount to solving self-consistently one Vlasov equation per particle species for the respective six-dimensional distribution function together with Maxwell's equations. For the study of micro-turbulence, this system includes many irrelevant spatio-temporal scales, however, and moreover, it is (still) inaccessible to well-resolved numerical simulations. To remedy this situation, the so-called (nonlinear) gyrokinetic approach [1] has been developed since the 1980s, which eliminates fast dynamics (like the gyromotion of the particles as well as plasma waves or compressional Alfvén waves) but retains the complete low-frequency physics, expressed in terms of five-dimensional distribution functions (the gyrophase-dependence is removed) and three scalar fluctuating fields (the electrostatic potential, the parallel component of

---

*Corresponding author
Email address:* `tbg@ipp.mpg.de` (T. Görler)

the vector potential, and the parallel component of the magnetic field). As it turns out, such a description is perfectly suited to study gradient-driven microturbulence in magnetized plasmas.

Various gyrokinetic codes have been developed since the 1990s (many of them are discussed, e.g., in Ref. [2]), differing primarily in the following ways: (1) the employed algorithms may be of Eulerian (grid-based), Lagrangian (particle-based), or semi-Lagrangian type – using a δf splitting or not; (2) the physics models may be reduced with respect to the full gyrokinetic system (neglecting, e.g., kinetic electrons and/or electromagnetic effects); (3) the geometry treatment may be based on realistic magnetohydrodynamic (MHD) equilibria or on simplified models; (4) the simulation domain may range from a (radially local) flux-tube to the full torus (including nonlocal effects); (5) the codes may be accessible only to the code authors or to a wider user community. The GENE code [3], which was first developed (starting in 1999) by F. Jenko [4] at IPP Garching, and later extended by various co-workers and collaborators (see, e.g., Refs. [5, 6, 7, 8, 9]), is a comprehensive Eulerian δf code (retaining full physics contents and geometry input) which is publicly available and has a world-wide user base. GENE is portable to a large number of supercomputer architectures and usually scales well up to the maximum number of available processors (see, e.g., Refs. [7, 10]). While the original version was restricted to a radially local flux-tube treatment, a full-torus (global) version of GENE has recently been developed in the context of a close collaboration of the authors of the present paper from IPP Garching and EPFL Lausanne. The key steps which were necessary for this extension will be described below.

Before that, a few more explanations concerning the differences between local and global simulations may be in place, however. Since the typical radial correlation lengths of turbulence driven by the most common microinstabilities like ion temperature gradient modes or trapped electron modes tend to be in the range of only several ion gyroradii (those of electron temperature gradient modes are still smaller), it seems justified to neglect radial variations of the background profiles and the magnetic geometry in the context of flux-tube simulations as long as the corresponding scale lengths are sufficiently disparate from the correlation lengths. This may be assumed to hold in the core region (except for discharges with internal transport barriers) of larger present-day or future tokamaks like JET or ITER, and to a significant degree also for medium-size machines like ASDEX Upgrade or DIII-D. Here, all profiles are evaluated just at a single radial position so that, e.g., temperatures and densities are constant throughout the whole radial simulation domain. First order derivatives appearing explicitly in the gyrokinetic equations are kept as well in order to retain, e.g., the linear gradient drive terms, as can be justified by means of a multiscale approach. For convenience, periodic boundary conditions are then often used in the radial direction, automatically keeping the (average) background gradients fixed and facilitating the use of spectral techniques. The latter, in turn, allow for a simple and very accurate computation of corresponding derivatives and operators in the gyrokinetic equations as will be shown later. With all these simplifications, however, one implicitly assumes a gyro-Bohm transport scaling, i.e. a Bohm scaling reduced by the gyroradius-to-machine-size ratio ρ^* where the latter has to be small. In order to determine the limit of such a-priori scalings and in order to capture meso-scale effects like heat flux avalanches (see, for instance, Refs. [11, 12, 13, 14]) one thus has to rely on global (as opposed to local) codes where the radial simulation box sizes can extend up to the full machine size, therefore covering full radial temperature, density and geometry profiles. In this case, periodic boundary conditions are inappropriate and have to be replaced, leading to major changes in the underlying numerical schemes. Nevertheless, as the correct prediction of the transport scaling represents a crucial task for the development of future fusion devices, sufficient motivation is provided to tackle this effort – in particular, as most of the existing global simulation results have been obtained employing reduced physics, e.g., adiabatic electrons.

The aim of the present paper is to describe the corresponding modifications of the previously

solely local GENE code (for some additional details, see Refs. [15, 16]) in order to meet the aforementioned requirements for the investigation of nonlocal effects. It is organized as follows. In the next section, the basic equations will be presented. In Sec. 3, the numerical implementations are discussed, followed by presentations of verification and validation studies in Sec. 4. Finally, a summary and conclusions are detailed in Sec. 5.

2. Theoretical background

2.1. Gyrokinetics

Both theoretical considerations and experimental observations indicate that the turbulent fluctuations of various plasma quantities in the core of fusion experiments obey the so-called gyrokinetic ordering [1]. According to the latter, the fluctuations are highly anisotropic (the parallel correlation lengths typically exceed the perpendicular ones by 2-3 orders of magnitude), of small amplitude (compared to the respective mean values), and of low frequency in relation to the gyrofrequency:

$$\frac{k_\parallel}{k_\perp} \sim \frac{q\phi_1}{T} \sim \frac{n_1}{n} \sim \frac{T_1}{T} \sim \frac{B_1}{B} \sim \frac{\omega}{\Omega} \sim \epsilon \ll 1. \quad (1)$$

Here, $k_\parallel$ and $k_\perp$ denote, respectively, the characteristic wave numbers parallel and perpendicular to the background magnetic field, q is the charge, ϕ_1, n_1, T_1, and B_1 the fluctuating parts of the electrostatic field ϕ, the density n, the temperature T and the magnetic field B. Furthermore, ω denotes a characteristic fluctuation frequency, $\Omega = |q| B/(mc)$ is the gyrofrequency and ϵ is a smallness parameter. In addition, the perpendicular turbulence length scales typically satisfy

$$\frac{\rho}{L_G} \sim \epsilon \ll 1, \quad (2)$$

with the gyroradius $\rho = \sqrt{T/m}/\Omega$ and the characteristical gradient length L_G of temperature, density, and magnetic field. Based on those orderings, it is reasonable to employ a reduced description of the particle dynamics, i.e., to find – e.g., with the help of Lie perturbation methods [1] – a set of coordinates for which the gyroangle

remains a cyclic variable even in the presence of fluctuating fields. The fast particle gyromotion in a nearly constant background field can thus be substituted by a gyro-ring description, so that the six-dimensional set of particle space and velocity coordinates $(\mathbf{x}, \mathbf{v})$ is replaced by five so-called gyrocenter coordinates $(\mathbf{X}, \mu, v_\parallel)$ where $\mathbf{X}$ is the gyrocenter position, $\mu = mv_\perp^2/(2B)$ is the magnetic moment, and $v_\parallel/v_\perp$ are the velocity components parallel/perpendicular to the magnetic field.

2.2. The gyrokinetic Vlasov equation

The accordingly transformed so-called full-f Vlasov equation of the species σ then reads [1]

$$\frac{\partial F_\sigma}{\partial t} + \frac{d\mathbf{X}}{dt} \cdot \nabla F_\sigma + \frac{dv_\parallel}{dt}\frac{\partial F_\sigma}{\partial v_\parallel} + \frac{d\mu}{dt}\frac{\partial F_\sigma}{\partial \mu} = 0 \quad (3)$$

in advection equation form, with

$$\frac{d\mathbf{X}}{dt} = v_\parallel \hat{\mathbf{b}}_0 + \frac{B_0}{B_{0\parallel}^*}\left(\mathbf{v}_{\bar{\xi}} + \mathbf{v}_{\nabla B} + \mathbf{v}_c\right),$$

$$\frac{dv_\parallel}{dt} = -\frac{d\mathbf{X}/dt}{m_\sigma v_\parallel} \cdot \left(q_\sigma \nabla \bar{\phi}_1 + \frac{q_\sigma}{c}\hat{\mathbf{b}}_0 \frac{\partial \bar{A}_{1\parallel}}{\partial t} + \mu \nabla B_0\right),$$

and

$$\frac{d\mu}{dt} = 0 \quad (4)$$

in the low β limit where the thermal to magnetic pressure ratio $\beta \equiv 8\pi p_0/B_0^2$ is less than a few percent as in most present-day tokamaks. Here, B_0 denotes the modulus of the magnetic field vector $\mathbf{B}_0$, $\hat{\mathbf{b}}_0 = \mathbf{B}_0/B_0$ the corresponding unit vector, $B_{0\parallel}^* = \hat{\mathbf{b}} \cdot \mathbf{B}_0^*$ the parallel component of $\mathbf{B}_0^* = \mathbf{B}_0 + \nabla \times (\mathbf{B}_0 v_\parallel/\Omega)$, $\bar{\xi}_1 = \bar{\phi}_1 - \frac{v_\parallel}{c}\bar{A}_{1\parallel}$ the gyroaveraged modified potential, $\mathbf{v}_{\bar{\xi}} = \frac{c}{B_0^2}\mathbf{B}_0 \times \nabla \bar{\xi}_1$ the generalized $\mathbf{E} \times \mathbf{B}$ velocity, $\mathbf{v}_{\nabla B_0} = \frac{\mu c}{q_\sigma B_0^2}\mathbf{B}_0 \times \nabla B_0$ the gradient-B velocity, and $\mathbf{v}_c = \frac{v_\parallel^2}{\Omega_\sigma}\left(\nabla \times \hat{\mathbf{b}}_0\right)_\perp$ the curvature drift velocity which can alternatively be expressed as $\mathbf{v}_c = \frac{v_\parallel^2}{\Omega_\sigma}\left(\hat{\mathbf{b}}_0 \times \left[\frac{\nabla B_0}{B_0} + \frac{\beta}{2}\frac{\nabla p_0}{p_0}\right]\right)$. Overbars denote gyroaverages being defined as

$$\bar{\phi}_1(\mathbf{X}) \equiv \mathcal{G}\left[\phi_1(\mathbf{X})\right] \equiv \frac{1}{2\pi}\oint d\theta \, \phi_1(\mathbf{X} + \mathbf{r}(\theta)) \quad (5)$$

3

with the gyroaverage operator $\mathcal{G}$ and the gyroradius vector $\mathbf{r}(\theta)$ being orthogonally aligned to the magnetic field.

The gyrokinetic Vlasov equation can be rewritten and also further simplified in the context of a δf splitting of the total distribution function into an equilibrium part F_0 – here, a local Maxwellian – and a fluctuating part F_1. According to the gyrokinetic ordering, one has $F_1/F_0 \sim \epsilon$ which can be applied to Eq. (3). Hence, keeping only first order terms in ϵ, the $\nabla \xi \times \mathbf{B}$ nonlinearity is retained while higher-order terms like the so-called $v_\parallel$-nonlinearity are neglected in line with careful studies in Refs. [17, 18, 19]. Finally, a new variable

$$g_{1\sigma} = F_{1\sigma} - \frac{q_\sigma}{m_\sigma c} \bar{A}_{1\parallel} \frac{\partial F_{0\sigma}}{\partial v_\parallel} \qquad (6)$$

will be used in the following in order to combine the two time derivatives appearing in Eq. (3).

2.2.1. Field aligned coordinates

Taking advantage of the anisotropic character of the turbulent fluctuations, the GENE code utilizes a field aligned coordinate system (x, y, z) in which x is a radial coordinate acting as a flux-surface label, z is a parallel coordinate, and y is a binormal coordinate. Given that the parallel correlation lengths exceed the perpendicular ones by 2-3 orders of magnitude, this procedure helps to save a respective number of grid points compared to a simple geometry setup ignoring this feature. The x and y directions are related to the equilibrium field via the relation

$$\mathbf{B}_0 = \mathcal{C}(x)\nabla x \times \nabla y . \qquad (7)$$

where $\mathcal{C}(x)$ is a transformation function which generally depends on the flux surface and which is defined by the specific MHD equilibrium. The corresponding Jacobian and the metric read

$$J^{-1} = (\nabla x \times \nabla y) \cdot \nabla z = \frac{\mathbf{B}_0 \cdot \nabla z}{\mathcal{C}(x)} \qquad (8)$$

and

$$g = (g^{ij}) = (\nabla u^i \cdot \nabla u^j) \qquad (9)$$

with $i, j = (1, 2, 3)$ and $u^{(1,2,3)} = (x, y, z)$. Furthermore, the combined metric coefficients $\gamma_1 = g^{xx}g^{yy} - g^{xy}g^{yx}$, $\gamma_2 = g^{xx}g^{yz} - g^{yx}g^{xz}$ and $\gamma_3 = g^{xy}g^{yz} - g^{yy}g^{xz}$ will be used in the following sections. More details may be found, e.g., in Refs. [20, 15, 16].

2.2.2. Normalization

In the context of numerical simulations, appropriately normalized equations are generally called for. Here, all physical quantities will be expressed in terms of a dimensional quantity usually identifiable by the index 'ref' and a dimensionless prefactor, earmarked with a hat. The basic reference values are the elementary charge e, a reference mass m_{ref}, a reference temperature T_{ref}, a (macroscopic) reference length L_{ref} and a reference magnetic field B_{ref}, so that e.g. the charge of the σth species can be written as $q_\sigma = e\hat{q}_\sigma$. Moreover, some composed quantities are used, which are the reference velocity $c_{\text{ref}} = \sqrt{T_{\text{ref}}/m_{\text{ref}}}$, the reference gyrofrequency $\Omega_{\text{ref}} = eB_{\text{ref}}/(m_{\text{ref}}c)$, the reference gyroradius $\rho_{\text{ref}} = c_{\text{ref}}/\Omega_{\text{ref}}$ and the reference thermal to magnetic pressure ratio $\beta_{\text{ref}} = 8\pi n_{\text{ref}} T_{\text{ref}}/B_{\text{ref}}^2$. With those definitions, the gyrocenter coordinates and time are normalized as listed in Table 1 where $v_{T\sigma}(x) = \sqrt{2T_{0\sigma}(x)/m_\sigma} =$

Table 1: Normalization of the gyrocenter coordinates and time

x	y	z	$v_\parallel$	μ	t
ρ_{ref}	ρ_{ref}	1	$v_{T\sigma}(x_0)$	$T_{0\sigma}(x_0)/B_{\text{ref}}$	$L_{\text{ref}}/c_{\text{ref}}$

$c_{\text{ref}} \hat{v}_{T\sigma}(x)$ denotes the thermal velocity of the σth species at radial position x. While on the one hand, a separation of scales due to different masses has been taken into account, it is not desirable to normalize the velocity space coordinates to radially dependent temperature profiles since such an approach would require additional interpolation schemes in corresponding derivatives or integrations. Thus, temperatures in velocity space normalization factors are just taken at a reference position x_0 which may for instance correspond to the center of the simulation domain or the position at which the profiles reach half

4

of their maximum. However, their species dependence is still taken into account which allows for a velocity space adaption to highly separated temperature profiles which might for instance happen during strong electron heating. Finally, it should be noted that the parallel coordinate z is considered to be dimensionless (angle-like), the corresponding length scale hence appears in the metric normalization.

The potentials, fields and distribution functions are chosen to be expressed as shown in Table 2 where again radial dependencies are only present

Table 2: Normalizations of the fields and the distribution functions

ϕ_1	$A_{1\parallel}$	$F_{0\sigma}$	$F_{1\sigma}$
$\dfrac{T_{\mathrm{ref}}}{e}\dfrac{\rho_{\mathrm{ref}}}{L_{\mathrm{ref}}}$	$\rho_{\mathrm{ref}}B_{\mathrm{ref}}\dfrac{\rho_{\mathrm{ref}}}{L_{\mathrm{ref}}}$	$\dfrac{n_{0\sigma}(x_0)}{v_{T\sigma}^3(x_0)}$	$\dfrac{\rho_{\mathrm{ref}}}{L_{\mathrm{ref}}}\dfrac{n_{0\sigma}(x_0)}{v_{T\sigma}^3(x_0)}$

in the normalized distribution functions itself. For further clarification, the normalized equilibrium part shall be given explicitly considering the previously mentioned local Maxwellian

$$\hat{F}_{0\sigma}(\mathbf{x}) = \frac{\hat{n}_{p\sigma}(x)}{[\pi\hat{T}_{p\sigma}(x)]^{3/2}}\,\mathrm{e}^{-\frac{\hat{v}_\parallel^2+\hat{\mu}\hat{B}_0(\mathbf{x})}{\hat{T}_{p\sigma}(x)}}, \qquad (10)$$

where additional abbreviations have been introduced for density and temperature profiles which are normalized to their value at the reference position x_0, $\hat{n}_{p\sigma} = n_{0\sigma}(x)/n_{0\sigma}(x_0)$ and $\hat{T}_{p\sigma} = T_{0\sigma}(x)/T_{0\sigma}(x_0)$. Finally, the (combined) metric coefficients are given in the units being presented in Table 3.

Table 3: Normalizations of the combined metric coefficients and further geometry related factors

γ_1	γ_2	γ_3	J	$\mathcal{C}$
1	$1/L_{\mathrm{ref}}$	$1/L_{\mathrm{ref}}$	L_{ref}	B_{ref}

With the aforementioned approximations and definitions, the normalized version of the gyrokinetic Vlasov-equation, Eq. (3), reads

$$\begin{aligned}
\frac{\partial\hat{g}_{1\sigma}}{\partial\hat{t}} =&\,\mathcal{V}_{\xi,y}\partial_{\hat{y}}\hat{\bar{\xi}}_1 + \mathcal{V}_{\Gamma,x}\hat{\Gamma}_{\sigma,x} + \mathcal{V}_{\Gamma,y}\hat{\Gamma}_{\sigma,y} \\
&- \frac{\hat{B}_0}{\hat{B}_{0\parallel}^*}\frac{1}{\hat{\mathcal{C}}}\left(\partial_{\hat{x}}\hat{\bar{\xi}}_1\hat{\Gamma}_{\sigma,y} - \partial_{\hat{y}}\hat{\bar{\xi}}_1\hat{\Gamma}_{\sigma,x}\right) \\
&+ \mathcal{V}_{\Gamma,z}\hat{\Gamma}_{\sigma,z} + \mathcal{V}_{F_1,v_\parallel}\frac{\partial\hat{F}_{1\sigma}}{\partial\hat{v}_\parallel} + \mathcal{V}_{F_0}\hat{F}_{0\sigma} \quad (11)
\end{aligned}$$

with the abbreviations

$$\hat{\Gamma}_{\sigma,i} = \partial_i\hat{F}_{1\sigma} + \frac{\hat{q}_\sigma}{\hat{T}_{0\sigma}}\hat{F}_{0\sigma}\partial_i\hat{\bar{\phi}}_1. \qquad (12)$$

and

$$\frac{\hat{B}_{0\parallel}^*}{\hat{B}_0} = 1 + \beta_{\mathrm{ref}}\sqrt{\frac{\hat{m}_\sigma\hat{T}_{0\sigma}(x_0)}{2}}\frac{\hat{j}_{0\parallel}}{\hat{q}_\sigma\hat{B}_0^2}\hat{v}_\parallel \qquad (13)$$

where the equilibrium current density $j_{0\parallel}$ is normalized to $en_{\mathrm{ref}}c_{\mathrm{ref}}$. The first term on the right hand side of Eq. (11) including the prefactor

$$\mathcal{V}_{\xi,y} = -\frac{1}{\hat{\mathcal{C}}}\frac{\hat{B}_0}{\hat{B}_{0\parallel}^*}\left[\frac{L_{\mathrm{ref}}}{L_{n_\sigma}} + \frac{L_{\mathrm{ref}}}{L_{T_\sigma}}\left(\frac{\hat{v}_\parallel^2+\hat{\mu}\hat{B}_0}{\hat{T}_{p\sigma}} - \frac{3}{2}\right)\right]\hat{F}_{0\sigma}$$

represents the linear drive term which is a function of the logarithmic radial density and temperature background gradients, $L_{n_\sigma}^{-1}(x') = -\partial_x\ln n_{0\sigma}|_{x'}$, and $L_{T_\sigma}^{-1}(x') = -\partial_x\ln T_{0\sigma}|_{x'}$. In local codes where the gyroradius is considered to be infinitesimally small compared to the tokamak minor radius, i.e. $\rho^* = \rho/a \to 0$, those gradients and all other (slowly) radially varying equilibrium functions $A(x)$ are now evaluated at a single flux surface at $x = x_0$ following the approximation

$$\begin{aligned}
A(x) =&\, A(x_0) + \frac{\partial A}{\partial(x/L_{\mathrm{ref}})}\bigg|_{x_0}\frac{x-x_0}{L_{\mathrm{ref}}} \\
\sim&\, A(x_0) + \frac{\partial A}{\partial(x/L_{\mathrm{ref}})}\bigg|_{x_0}\mathcal{O}(\rho^*).
\end{aligned}$$

However, in the global code, radial variations being in line with the aforementioned orderings are taken into account instead. The linear drive is

5

thus a function of the radial coordinate. The second and third term contain the the combined curvature and gradient-B prefactors

$$\mathcal{V}_{\Gamma,x} = -\frac{\hat{T}_{0\sigma}(x_0)}{\hat{q}_\sigma} \frac{\hat{\mu}\hat{B}_0 + 2\hat{v}_\parallel^2}{\hat{B}_{0\parallel}^*} \hat{K}_x,$$

and

$$\mathcal{V}_{\Gamma,y} = -\frac{\hat{T}_{0\sigma}(x_0)}{\hat{q}_\sigma \hat{B}_{0\parallel}^*} \left[(\hat{\mu}\hat{B}_0 + 2\hat{v}_\parallel^2)\hat{K}_y - \beta_{\text{ref}} \frac{\hat{v}_\parallel^2 \hat{p}_0}{\hat{\mathcal{C}} \, \hat{B}_0} \frac{L_{\text{ref}}}{L_p} \right],$$

with the gradients of the equilibrium magnetic field $\hat{K}_x = -\frac{1}{\hat{\mathcal{C}}} \frac{L_{\text{ref}}}{B_{\text{ref}}} \left(\frac{\partial B_0}{\partial y} + \frac{\gamma_2}{\gamma_1} \frac{\partial B_0}{\partial z} \right)$ and $\hat{K}_y = \frac{1}{\hat{\mathcal{C}}} \frac{L_{\text{ref}}}{B_{\text{ref}}} \left(\frac{\partial B_0}{\partial x} - \frac{\gamma_3}{\gamma_1} \frac{\partial B_0}{\partial z} \right)$ and the logarithmic background pressure gradient $L_p^{-1} = -\partial_x \ln p_0(x)$. The remaining prefactors succeeding the nonlinearity (term 4 and 5) in Eq. (11) are the parallel derivative prefactor

$$\mathcal{V}_{\Gamma,z} = -\hat{v}_{T\sigma}(x_0) \frac{\hat{\mathcal{C}}}{\hat{J}\hat{B}_0} \hat{v}_\parallel,$$

the trapping term prefactor

$$\mathcal{V}_{F_1,v_\parallel} = \frac{\hat{v}_{T\sigma}(x_0)}{2} \frac{\hat{\mathcal{C}}}{\hat{J}\hat{B}_0} \hat{\mu}\partial_{\hat{z}}\hat{B}_0,$$

and the F_0 contribution term

$$\mathcal{V}_{F_0} = \frac{\hat{T}_{0\sigma}(x_0)}{\hat{q}_\sigma} \frac{\hat{\mu}\hat{B}_0 + 2\hat{v}_\parallel^2}{\hat{B}_{0\parallel}^*} \hat{K}_x$$
$$\cdot \left[\frac{L_{\text{ref}}}{L_{n_\sigma}} + \frac{L_{\text{ref}}}{L_{T_\sigma}} \left(\frac{\hat{v}_\parallel^2 + \hat{\mu}\hat{B}_0}{\hat{T}_{p\sigma}} - \frac{3}{2} \right) \right],$$

stemming from the gradient-B and curvature drifts being multiplied with ∇F_0. In the current code version, the local Maxwellian is considered as an exact equilibrium distribution and the above term is thus neglected, hence following an often employed approach, see Ref. [21] and the discussion therein. The generalization to, e.g, a canonical Maxwellian or to precomputed neoclassical equilibria will be addressed in a future work. Anyway, linear simulations are not affected as this term just acts on the $k_y = 0$ mode in axisymmetric devices. Furthermore, even nonlinear

simulations using this approximation can exhibit an amazing level of agreement compared to simulations with a canonical Maxwellian as has been demonstrated in Ref. [22].

2.3. The gyrokinetic field equations

2.3.1. Velocity space moments of the particle distribution function

Both in order to solve Maxwell's equations (which are employed to determine the perturbed fields self-consistently) as well as for diagnostic purposes, velocity space moments of the distribution functions – expressed in particle coordinates – are required. Hence, the following considerations prove useful. Starting with the definition of the ath moment in $v_\parallel$ and the bth moment in $v_\perp$,

$$M_{ab,\sigma}(\mathbf{x}) = \int \mathrm{d}^3 v \, v_\parallel^a v_\perp^b f_\sigma(\mathbf{x}, \mathbf{v}), \qquad (14)$$

one arrives at the guiding-center formulation by applying the previously introduced transformation

$$M_{ab,\sigma}(\mathbf{x}) = \int \mathrm{d}^3 X \mathrm{d}v_\parallel \mathrm{d}\mu \mathrm{d}\theta \, \mathcal{J} v_\parallel^a v_\perp^b \cdot$$
$$\delta(\mathbf{X} + \mathbf{r} - \mathbf{x}) F_{\sigma,\text{gc}}(\mathbf{X}, v_\parallel, \mu, \theta) \quad (15)$$

where the corresponding phase space Jacobian is given by $\mathcal{J} = \frac{1}{m^3}\sqrt{|(\omega_{\lambda\nu})|}$ with the determinant of the Lagrange tensor, see e.g. Ref. [23], $|\omega_{\lambda\nu}| = \left| \frac{\partial \bar{\Gamma}_{0,\nu}}{\partial Z^\lambda} - \frac{\partial \bar{\Gamma}_{0,\lambda}}{\partial Z^\nu} \right| = m^2 B_{0\parallel}^*$. Employing now a first-order pull-back operator [1] in order to use the gyrocenter instead of the guiding-center distribution function $F_{\sigma,\text{gc}}$ and considering a local Maxwellian as background distribution function yields to first order in ϵ

$$M_{ab,\sigma}(\mathbf{x}) = \pi \iint \mathrm{d}v_\parallel \mathrm{d}\mu' \, \mathcal{G}^\dagger \frac{B_{0\parallel}^*}{B_0} v_\parallel^a \, (\mu')^{\frac{b}{2}} \, v_{T\sigma}^{\frac{b}{2}+1} F_{1\sigma}$$
$$- q_\sigma \left\{ \frac{n_{0\sigma} v_{T\sigma}^{a+b}}{T_{0\sigma}} \Upsilon(a)\,(b/2)! \right.$$
$$\left. - \int \mathrm{d}\mu' \, \mathcal{G}^\dagger \frac{n_{0\sigma} v_{T\sigma}^{a+b}}{T_{0\sigma}} \Upsilon(a)\,(\mu')^{b/2} \, \mathrm{e}^{-\mu'} \mathcal{G} \right\} \phi_1 \quad (16)$$

with the abbreviation

$$\Upsilon(a) = \mathcal{I}(a) + \frac{8\pi T_{0\sigma}}{B_0^2} \frac{j_{0\parallel}}{q_\sigma v_{T\sigma}} \mathcal{I}(a+1) \qquad (17)$$

for the $v_\parallel$ integration where

$$\mathcal{I}(a) = \frac{1}{\sqrt{\pi}} \int_{-\infty}^{\infty} \mathrm{d}x \, x^a \mathrm{e}^{-x^2} = \begin{cases} 0, & a \text{ odd} \\ 1, & a = 0 \\ \frac{1 \cdot 3 \cdots (a-1)}{\sqrt{2}^a} & a \text{ even.} \end{cases} \qquad (18)$$

Here, $\mathcal{G}^\dagger$ denotes the adjoint operator of $\mathcal{G}$, which represents gyroaverages of the form $\mathcal{G}^\dagger F \equiv \frac{1}{2\pi} \oint \mathrm{d}\theta \, F(\mathbf{x} - \mathbf{r}(\theta))$ and $\mu' = \mu B_0/T_{0\sigma}$ has been introduced in order to improve the readability although the implementation is employing a μ grid.

2.3.2. The gyrokinetic Poisson equation

The perturbed electrostatic potential is linked to the perturbed charge density by means of the Poisson equation

$$-\nabla^2 \phi_1(\mathbf{x}) = 4\pi \sum_\sigma n_{1\sigma}(\mathbf{x}) q_\sigma \qquad (19)$$

where σ is running over all species and the density perturbation of the σth species $n_{1\sigma}(\mathbf{x}) = M_{00,\sigma}(\mathbf{x})$ is given by the $(0,0)$-velocity space moment of the distribution function $f_{1\sigma}(\mathbf{x}, \mathbf{v})$ in particle coordinates. Using Eq. (16) and considering the flute-like character of the turbulent fields, which allows to neglect parallel derivatives compared to perpendicular ones, leads to

$$\left\{ -\hat{\nabla}_\perp^2 \hat{\lambda}_D^2 + \sum_\sigma \hat{q}_\sigma^2 \left[\frac{\hat{n}_{0\sigma}}{\hat{T}_{0\sigma}} \mathbb{1} - \int \mathrm{d}\hat{\mu}' \, \mathcal{G}^\dagger \frac{\hat{n}_{0\sigma}}{\hat{T}_{0\sigma}} \mathrm{e}^{-\hat{\mu}'} \mathcal{G} \right] \right\} \hat{\phi}_1$$
$$= \sum_\sigma \hat{n}_{0\sigma}(x_0) \hat{q}_\sigma \pi \iint \mathrm{d}\hat{v}_\parallel \mathrm{d}\hat{\mu} \, \mathcal{G}^\dagger \hat{B}_0 \hat{F}_{1\sigma} \qquad (20)$$

in normalized units. Here, $\hat{\lambda}_D = \frac{\lambda_D}{\rho_{\mathrm{ref}}} = \sqrt{\frac{B_{\mathrm{ref}}^2}{4\pi n_{\mathrm{ref}} m_{\mathrm{ref}} c^2}}$ which can be identified as the normalized Debye length.

Adiabatic electrons. For basic investigations, the limit of massless/adiabatic electrons is often employed, in particular in order to lower the computational costs. In this case, fluctuations of the

electrostatic potential along the magnetic field lines are almost instantaneously balanced by the electrons which implies a modified adiabaticity relation

$$\frac{n_{1e}}{n_{0e}} = \frac{e}{T_{0e}} (\phi_1 - \langle \phi_1 \rangle_{\mathrm{FS}}). \qquad (21)$$

Here, $\langle \cdots \rangle_{\mathrm{FS}}$ denotes flux surface averaging [24] which is defined for an arbitrary function $f(\mathbf{x})$ as

$$\langle f \rangle_{\mathrm{FS}}(x) = \frac{\partial}{\partial V} \int_V \mathrm{d}V' f(\mathbf{x})$$
$$= \iint \mathrm{d}y \mathrm{d}z f(\mathbf{x}) J(\mathbf{x}) \mathrm{d}y \mathrm{d}z \bigg/ \iint J(\mathbf{x}). \qquad (22)$$

Considering in addition a vanishing electron gyroradius and Debye length and neglecting magnetic field fluctuations, the normalized Poisson equation in the adiabatic electron limit becomes

$$\hat{\phi}_1 = \left\{ \frac{\hat{n}_{0e}}{\hat{T}_{0e}} \mathbb{1} + \sum_{\sigma \neq e} \hat{q}_\sigma^2 \left[\frac{\hat{n}_{0\sigma}}{\hat{T}_{0\sigma}} \mathbb{1} - \int \mathrm{d}\hat{\mu}' \mathcal{G}^\dagger \frac{\hat{n}_{0\sigma}}{\hat{T}_{0\sigma}} \mathrm{e}^{-\hat{\mu}'} \mathcal{G} \right] \right\}^{-1}$$
$$\cdot \left[\pi \sum_{\sigma \neq e} \hat{n}_{0\sigma}(x_0) \hat{q}_\sigma \iint \mathrm{d}\hat{v}_\parallel \mathrm{d}\hat{\mu} \mathcal{G}^\dagger \hat{B}_0 \hat{F}_{1\sigma} + \mathbb{1} \frac{\hat{n}_{0e}}{\hat{T}_{0e}} \langle \hat{\phi}_1 \rangle_{\mathrm{FS}} \right].$$

The flux surface averaged potential is finally obtained by flux surface averaging the whole quasineutrality equation, thus erasing the electron contribution. Assuming a separate and independent treatment of operators and potentials, it is given by

$$\langle \hat{\phi}_1 \rangle_{\mathrm{FS}} = \pi \sum_{\sigma \neq e} \hat{n}_{0\sigma} \hat{q}_\sigma \left\langle \iint \mathrm{d}\hat{v}_\parallel \mathrm{d}\hat{\mu} \, \mathcal{G}^\dagger \hat{B}_0 \hat{F}_{1\sigma} \right\rangle_{\mathrm{FS}}$$
$$\cdot \left\{ \sum_{\sigma \neq e} \hat{q}_\sigma^2 \left[\frac{\hat{n}_{0\sigma}}{\hat{T}_{0\sigma}} \mathbb{1} - \left\langle \int \mathrm{d}\hat{\mu}' \mathcal{G}^\dagger \frac{\hat{n}_{0\sigma}}{\hat{T}_{0\sigma}} \mathrm{e}^{-\hat{\mu}'} \mathcal{G} \right\rangle_{\mathrm{FS}} \right] \right\}^{-1}. \qquad (23)$$

2.3.3. Ampère's law

Using the Coulomb gauge $\nabla \cdot \mathbf{A} = 0$ and neglecting any equilibrium electric field, Ampère's law can be expressed as

$$-\nabla_\perp^2 A_{1\parallel} = \frac{4\pi}{c} j_{1\parallel} = \frac{4\pi}{c} \sum_\sigma q_\sigma M_{10,\sigma}(\mathbf{x}). \qquad (24)$$

for the perturbed parallel component using the same approximations provided by the gyrokinetic ordering as, for instance, in the derivation of Poisson's equation. Replacing $M_{10,\sigma}(\mathbf{x})$ by its explicit representation given in Eq. (16) and changing to normalized quantities yields one arrives at the following normalized equation

$$
\begin{aligned}
&\left\{ -\hat{\nabla}_\perp^2 + \beta_{\mathrm{ref}} \sum_\sigma \hat{q}_\sigma^2 \int \mathrm{d}\hat{\mu}' \mathcal{G}^\dagger \frac{\hat{n}_{0\sigma}\mathcal{I}(2)}{\hat{m}_\sigma} \mathrm{e}^{-\hat{\mu}'} \mathcal{G} \right\} \hat{A}_{1\parallel} \\
&= \frac{\beta_{\mathrm{ref}}}{2} \sum_\sigma \hat{q}_\sigma \left\{ \hat{n}_{0\sigma}(x_0)\hat{v}_{T\sigma}(x_0)\pi \iint \hat{B}_{0\parallel}^* \hat{v}_\parallel \mathcal{G}^\dagger \hat{g}_{1\sigma} \mathrm{d}\hat{v}_\parallel \mathrm{d}\hat{\mu} \right. \\
&\quad \left. - \beta_{\mathrm{ref}} \left[\frac{\hat{n}_{0\sigma}\hat{j}_{0\parallel}}{\hat{B}_0^2}\mathcal{I}(2) - \int \mathrm{d}\hat{\mu}' \mathcal{G}^\dagger \frac{\hat{n}_{0\sigma}\hat{j}_{0\parallel}}{\hat{B}_0^2}\mathcal{I}(2) \mathrm{e}^{-\hat{\mu}'} \mathcal{G} \right] \hat{\phi}_1 \right\}
\end{aligned}
$$

$$(25)$$

where $\mathcal{I}(2)$ is typically evaluated numerically in order to avoid the so-called *Ampère cancellation problem* [25] which otherwise would stem from different treatments of the $v_\parallel$ integration on the left and right hand side of Eq. (25).

2.4. The collision operator

As mentioned before, the low densities and high temperatures of fusion plasmas lead to low collisionalities. For certain regimes, this may justify the use of a Vlasov treatment, focusing on indirect particle interactions via collectively generated fields and neglecting collisions altogether. In general, however, direct particle interactions, to lowest order binary collisions, constitute an important ingredient of the overall dynamics. Thus, an additional collision operator, here $C(F_\sigma, F_{\sigma'})$, is constructed and added to the right hand side of the kinetic equation,

$$
\frac{\partial F_\sigma}{\partial t} + \dot{\mathbf{X}} \cdot \nabla F_\sigma + \dot{\mu}\frac{\partial F_\sigma}{\partial \mu} + \dot{v}_\parallel \frac{\partial F_\sigma}{\partial v_\parallel} = \sum_{\sigma'} C(F_\sigma, F_{\sigma'}).
$$

$$(26)$$

In GENE, collisions are modeled using a Landau-Boltzmann collision operator,

$$
C(F_\sigma, F_{\sigma'}) = \frac{\partial}{\partial \mathbf{v}} \cdot \left(\overleftrightarrow{D} \cdot \frac{\partial}{\partial \mathbf{v}} - \mathbf{R} \right) F_\sigma \qquad (27)
$$

where $\overleftrightarrow{D}$ denotes a diffusion tensor

$$
\overleftrightarrow{D} = \frac{2\pi q_\sigma^2 q_{\sigma'}^2}{m_\sigma^2} \ln \Lambda_c \frac{\partial^2}{\partial \mathbf{v} \partial \mathbf{v}} \int \mathrm{d}^3 v' \, |\mathbf{v} - \mathbf{v}'| \, F_{\sigma'}
$$

$$(28)$$

with the Coulomb logarithm $\ln \Lambda_c$ (see, e.g., Ref. [26]), and the dynamical friction

$$
\mathbf{R} = \frac{4\pi q_\sigma^2 q_{\sigma'}^2}{m_\sigma \, m_{\sigma'}} \ln \Lambda_c \frac{\partial}{\partial \mathbf{v}} \int \mathrm{d}^3 v' \frac{F_{\sigma'}}{|\mathbf{v} - \mathbf{v}'|} . \qquad (29)
$$

Consistently with the δf approach, the collision operator is linearized as follows:

$$
\tilde{C} = C(F_{0\sigma}, F_{1\sigma'}) + C(F_{1\sigma}, F_{0\sigma'}).
$$

Further details can be found in Ref. [8].

2.5. Sources and sinks

In the absence of any explicit heat or particle source, the temperature and density profiles in a global nonlinear simulation tend to relax. The corresponding gradients eventually get close to their critical values, the turbulence drive is strongly decreased, and a state close to marginality is reached. The goal of adding sources and sinks is thus to maintain a quasi-steady state turbulence regime.

2.5.1. The Krook operator

When Dirichlet boundary conditions are considered in the radial direction for both the distribution function F_1, as well as the fluctuating fields ϕ_1 and $A_{\parallel 1}$, the temperature and density at both ends of the simulation domain are constrained to their initial values, while a profile relaxation occurs in the center of the domain. This may lead to strong, unphysical profile variations close to the boundaries, which in turn can generate strong turbulence in the edge of the simulation box. In order to avoid such behavior, an artificial Krook damping operator is applied in buffer regions. This operator is added to the right hand side of the gyrokinetic Vlasov equation (11) and is defined as

$$
\hat{h}_K = -\hat{\nu}_K(x) \, \hat{g}_{1\sigma}, \qquad (30)
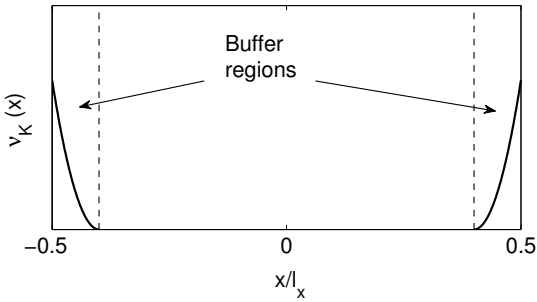$$

Figure 1: Coefficient profile $\hat{\nu}_k(x)$ of the damping Krook operator applied within edge buffer regions in nonlinear simulations.

where the profile function $\hat{\nu}_K(x)$ is zero outside of the buffer regions, and is typically determined by a fourth order polynomial ramp inside, as illustrated in Fig. 1. The maximal amplitude of ν_k is set to be comparable to the linear growth rates and the width of the buffer regions typically represents $5-10\%$ of the simulation domain on each sides.

2.5.2. The Krook-type heat source

In order to allow for quasi-steady state non-linear simulations, an artificial Krook-type heat source is implemented in addition. This source, similar to the one described in Ref. [27], is applied over the whole radial simulation domain and is designed to control the temperature profile, while conserving the flux-surface averaged density and parallel momentum. The following term is thus added to the right hand side of the gyrokinetic Vlasov equation (11):

$$\hat{\mathcal{S}}_K(x, |v_\parallel|, \mu) = -\hat{\gamma}_h \left[\langle \hat{F}_{1\sigma}(\mathbf{X}, |v_\parallel|, \mu) \rangle \right.$$
$$\left. -\langle \hat{F}_{0\sigma}(\mathbf{X}, |v_\parallel|, \mu) \rangle \frac{\langle \int d\mathbf{v} \, \langle \hat{F}_{1\sigma}(\mathbf{X}, |v_\parallel|, \mu) \rangle \rangle}{\langle \int d\mathbf{v} \, \langle \hat{F}_{0\sigma}(\mathbf{X}, v_\parallel, \mu) \rangle \rangle} \right],$$
(31)

where $\langle \ldots \rangle$ refers to the flux-surface average and

$$\hat{F}_{1\sigma}(\mathbf{X}, |v_\parallel|, \mu) = \frac{\hat{F}_{1\sigma}(\mathbf{X}, v_\parallel, \mu) + \hat{F}_{1\sigma}(\mathbf{X}, -v_\parallel, \mu)}{2} .$$
(32)

The conservation of density is ensured through the correction term $\langle \int \cdots \rangle / \langle \int \cdots \rangle$, while the conservation of parallel momentum is verified since

S_K is even in $v_\parallel$ as result of the symmetrization of the distribution with respect to this variable.

2.5.3. The localized heat source

The most realistic source model currently available in GENE is closely following the implementation being, e.g., described in Ref. [28] for the gyrokinetic turbulence code GYSELA [29]. It represents a localized heat source and is added to the right hand side of the Vlasov equation as follows

$$\frac{\mathrm{d}g}{\mathrm{d}t} = \mathcal{S}_H = \mathcal{S}_0 \hat{\mathcal{S}}_x \hat{\mathcal{S}}_E.$$
(33)

Here,

$$\hat{\mathcal{S}}_E = \frac{2}{3} \frac{1}{\hat{p}_{0\sigma}(x)} \left(\frac{\hat{E}}{\hat{T}_{p\sigma}} - \frac{3}{2} \right) \hat{F}_{0\sigma},$$
(34)

with $\hat{E} = \left(\hat{v}_\parallel^2 + \hat{\mu} \hat{B}_0 \right)$, denotes an energy source term being normalized such that $\pi \hat{B}_0 \hat{p}_{0\sigma}(x_0) \int \mathrm{d}\hat{v}_\parallel \mathrm{d}\hat{\mu} \, \hat{E} \hat{\mathcal{S}}_E = 1$. This choice ensures that neither particle nor momentum are injected as can be confirmed by computing the according moments. In addition, a radial source profile $\mathcal{S}_{x,in}(\hat{x})$, e.g. a Gaussian shape, can be freely defined by the user. It is then normalized according to

$$\hat{\mathcal{S}}_x(\hat{x}) = \mathcal{S}_{x,in}(\hat{x}) / \int \mathrm{d}^3\hat{x} \, \mathcal{S}_{x,in}(\hat{x}) \hat{J}(\hat{x}, \hat{z}). \quad (35)$$

Finally, an amplitude $\mathcal{S}_0$ which is given in units of $n_{0\sigma}(x_0)\rho_{\mathrm{ref}} c_{\mathrm{ref}}/(v_{T\sigma}^3(x_0)L_{\mathrm{ref}}^2)$ can be specified. The total injected power is thus

$$P_{\mathrm{add}} = \mathcal{S}_0 \int \mathrm{d}^3x \int \mathrm{d}^3v E \, \hat{\mathcal{S}}_x \hat{\mathcal{S}}_E$$
$$= \hat{\mathcal{S}}_0 n_{\mathrm{ref}} T_{\mathrm{ref}} \rho_{\mathrm{ref}}^3 \, c_{\mathrm{ref}}/L_{\mathrm{ref}}.$$
(36)

2.6. Equilibrium models

So far, no explicit expressions have been given for the different geometrical terms appearing in Eq. (11) which are related to the actually chosen magnetic equilibrium. In an axisymmetric system, as is currently considered in the global version of the code, the field aligned coordinates (x, y, z) can be obtained from the straight field

9

line coordinate system (Ψ, χ, ϕ), where Ψ is the poloidal flux function, χ the generalized poloidal angle and ϕ the toroidal angle through the relations:

$$x = C_x(\Psi) - x_0 \, , \ y = C_y(q\chi - \phi) - y_0 \, , \ z = \chi \, . \tag{37}$$

with the coefficients functions C_x and C_y such that $\mathcal{C}(x) = (\frac{dC_x(x)}{d\Psi} C_y)^{-1}$.

For many applications, it can be useful to consider a simple analytical equilibrium, and a circular concentric flux surface model is thus implemented in the code. Considering Solovev-type solutions of the Grad-Shafranov equation [30] in the large aspect ratio limit $R_0/a \gg 1$, where R_0 and a are respectively the major and minor tokamak radii, the equilibrium poloidal flux function can be expressed as $\Psi = \Psi_{\text{edge}}(r/a)^2$. Here, r is the radius local to a given flux surface as illustrated in Fig. 2.6. In this limit, the magnetic surfaces thus have a circular cross section, and the magnetic field is given by

$$\mathbf{B}_0 = \frac{R_0 \, B_{\text{ref}}}{R} \left[\mathbf{e}_\phi + \frac{r}{R_0 \, \bar{q}} \, \mathbf{e}_\theta \right] \, , \tag{38}$$

where B_{ref} is the magnetic field at the magnetic axis, and $\bar{q}$ is a pseudo safety factor which can be related to the real safety factor according to

$$q(r) = \frac{1}{2\pi} \int_0^{2\pi} \mathrm{d}\theta \, \frac{\mathbf{B}_0 \cdot \nabla\phi}{\mathbf{B}_0 \cdot \nabla\theta} \ = \frac{\bar{q}(r)}{\sqrt{1 - \epsilon^2}} \, , \tag{39}$$

with the inverse aspect ratio $\epsilon = r/R_0$. This pseudo safety factor profile $\bar{q} = \bar{q}(r)$ is motivated by the ad-hoc relation $d\Psi/dr = B_{\text{ref}} \, r/\bar{q}(r)$ and occasionally used instead of $q(r)$ as input parameter in intercode benchmarks. However, the straight field line angle χ is defined such that $(\mathbf{B}_0 \cdot \nabla\phi)/(\mathbf{B}_0 \cdot \nabla\chi) = q$, which leads to the $q(r)$ dependent relation $d\chi/d\theta = \mathbf{B}_0 \cdot \nabla\phi/(q \, \mathbf{B}_0 \cdot \nabla\theta)$. Integrating over θ yields

$$\chi(r, \theta) = \frac{1}{q} \int_0^\theta \mathrm{d}\theta' \, \frac{\mathbf{B}_0 \cdot \nabla\phi}{\mathbf{B}_0 \cdot \nabla\theta'}$$
$$= 2 \arctan \left[\sqrt{\frac{1 - \epsilon}{1 + \epsilon}} \tan \left(\frac{\theta}{2} \right) \right] . \tag{40}$$
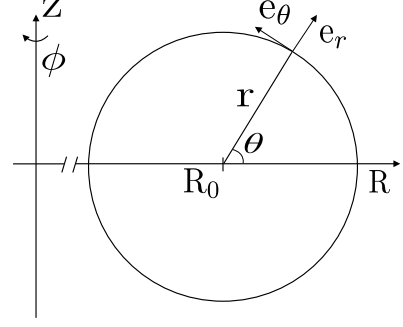

Figure 2: Circular flux surface in toroidal coordinates (r, θ, Φ).

From these definitions for Ψ and χ, the metric tensor $g^{\alpha\beta} = \nabla\alpha \cdot \nabla\beta$ in (Ψ, χ, ϕ) is obtained from the known metric in the (r, θ, ϕ) coordinate system, leading to

$$g^{\Psi\Psi} = \frac{B_{\text{ref}}^2 \, r^2}{\bar{q}^2} \, , \ g^{\chi\chi} = \frac{1}{r^2} \left[\frac{R_0^2 \bar{q}^2}{R^2 q^2} + \frac{\epsilon^2 \sin^2 \chi}{(1 - \epsilon^2)^2} \right] \, ,$$
$$g^{\Psi\chi} = -\frac{B_{\text{ref}} \epsilon}{\bar{q}} \frac{\sin \chi}{(1 - \epsilon^2)} \, , \ g^{\phi\phi} = \frac{1}{R^2} \, ,$$
$$g^{\Psi\phi} = g^{\chi\phi} = 0 \, . \tag{41}$$

With those relations, the metric tensor in the field aligned coordinates (x, y, z) can finally be derived to be

$$g^{xx} = \left(\frac{dC_x}{d\Psi} \right)^2 g^{\Psi\Psi} \, , \ g^{zz} = g^{\chi\chi} \, ,$$
$$g^{xy} = \frac{dC_x}{d\Psi} C_y \left(q'\chi g^{\Psi\Psi} + q g^{\Psi\chi} \right) \, ,$$
$$g^{yy} = C_y^2 \left[(q')^2 \chi^2 g^{\Psi\Psi} + 2qq'\chi \, g^{\Psi\chi} + q^2 g^{\chi\chi} + g^{\phi\phi} \right] \, ,$$
$$g^{xz} = \frac{dC_x}{d\Psi} g^{\Psi\chi} \, , \quad g^{yz} = C_y \left(q'\chi \, g^{\Psi\chi} + q \, g^{\chi\chi} \right) \, . \tag{42}$$

When using this circular analytical model, the x variable is chosen as $x = r - x_0$, i.e. $dC_x/d\Psi = \bar{q}/(r \, B_{\text{ref}})$, and $C_y = r_0/q_0$. Note, that the presented equilibrium model differs from the standard implementation of the $s - \alpha$ model as all terms in ϵ are retained here [20].

In order to investigate more realistic equilibria, interfaces with the MHD equilibrium code CHEASE [31] or the field line tracer TRACER [32] can alternatively be used.

10

3. Numerical implementation

Having discussed the theoretical framework, the present section is dedicated to the discussion of the numerical schemes which are used to discretize the gyrokinetic system of equations.

Following the method of lines [33], the distribution function and the fields are first discretized on a fixed grid in phase space while the time variable is left continuous. The hyperbolic integro-differential system of equations is thus reduced to a system of ordinary differential equations which can then be solved using, e.g., a standard Runge-Kutta method.

3.1. Eigenvalue and initial value solver

Often, gyrokinetic investigations involve a careful study of the linear properties of the existing microinstabilities, determining, for instance, their growth rates and real frequencies. For linear investigations, all relevant terms in the gyrokinetic Vlasov equation can be cast into an operator acting on a state vector representing the distribution function. Using iterative eigenvalue solvers provided by the SLEPC [34, 35] extension of the PETSC [36, 37, 38] package then allows for the analysis of the full eigenvalue spectrum or of parts thereof. These libraries are also employed to determine the maximum linear time step for initial value calculations based on explicit time schemes. Concerning the latter, several options are at hand. Besides standard Runge-Kutta schemes of 3rd and 4th order, a numerically optimized 6-stage, 4th order Runge-Kutta scheme as proposed in [39] is available as well. A more detailed discussion can be found in [8].

3.2. Flux tube approach and boundary conditions

The flute-like character of plasma microturbulence – already mentioned in the context of the gyrokinetic ordering – allows for a minimization of the simulation volume and thus of the computational costs. Local codes, for instance, usually consider a flux-tube domain whose length corresponds to one poloidal turn [40, 41, 42]. The appropriate boundary conditions will be discussed in the following since they are linked to the ones used in the global GENE version.

3.2.1. Radial boundary condition

Periodic boundary conditions, $f(x, y, z) = f(x + L_x, y, z)$ (here, f denotes an arbitrary function), as they are typically implemented in local codes can still be used in the global version for comparisons. However, such a choice is not applicable in global computations since radial and in general non-periodic variations of equilibrium quantities shall be kept. Thus, GENE is currently equipped with two alternatives. Either, all quantities are held fixed at the boundaries $\mathcal{B}$ using Dirichlet type conditions, $f(x, y, z)|_{x \in \mathcal{B}} = 0$, or floating temperatures and density profiles are allowed. The latter is achieved by employing von Neumann type conditions, $\partial_x f(x, k_y = 0, z)|_{x \in \mathcal{B}} = 0$ for the constant part in the y direction ($k_y = 0$) and else ($k_y \neq 0$) the aforementioned Dirichlet type conditions such that particle and heat fluxes vanish at the boundaries. In the present version of the code, these conditions are applied to both gyrocenter and particle coordinate representations in the same manner. It should be mentioned at this point that the effect of the boundary conditions is expected to penetrate some distance into the simulation domain. The associated characteristical length scale naturally depends on ρ^* and on the strength of the radial coupling being, for instance, caused by radial derivatives and the gyroaveraging procedure.

3.2.2. Boundary condition in the binormal direction

In the y direction, often called binormal (referring to the orthogonal vectors $(\hat{\mathbf{e}}^x, \hat{\mathbf{e}}^y, \hat{\mathbf{e}}_z)$ at outboard midplane) or toroidal (with respect to the alignment of the corresponding covariant basis vector $\hat{\mathbf{e}}_y$) direction, periodic boundary conditions are taken in the local as well as the global GENE code which is well justified for axisymmetric devices. Within the flux tube concept the box size might, however, be restricted to an integer fraction (inverse toroidal mode number n_0) of the full flux surface. Here, periodicity can still be assumed if the box size L_y is larger than a few correlation lengths of the turbulence structures to be investigated. As pointed out in Ref. [43], such an approach corresponds to a thinning out of mode

numbers in the y direction as becomes obvious if a Fourier transformation

$$f(x, k_y, z) = \frac{1}{L_y} \int_0^{L_y} dy\, e^{-ik_y y}\, f(x, y, z) \quad (43)$$

is applied. Here, the discretized mode number spectrum is given by $k_y = k_y^{\min} \cdot j$ with $k_y^{\min} = 2\pi/L_y = n_0/C_y$ and j being integer-valued. Thus, increasing the toroidal mode number n_0 similarly increases $k_y^{\min}$ or – if $k_y^{\min}$ shall be kept constant – the possible j values are restricted to $j = n_0 \cdot l$ with $l = 0, 1, 2, \ldots$. The implementation in GENE is based on such a Fourier representation in the y direction to allow for the application of spectral methods.

3.2.3. Parallel boundary condition

Obviously, a thin flux tube in an axisymmetric equilibrium which extends for one poloidal turn is characterized by exactly the same geometric quantities at both ends. However, it is clear that these ends do not physically match for non-integer q values, and that finite magnetic shear induces a tilting of the simulation box. An additional x and y dependent phase factor is thus introduced [42] in order to compensate for those effects. The parallel (z) boundary condition then reads

$$f(x, k_y, z + L_z) = f(x, k_y, z) \exp\left(-2\pi i n_0 q(x) j\right) \quad (44)$$

where j denotes, as before, the integer-valued index of the k_y mode and n_0 is the aforementioned toroidal mode number. At this point it should be noted that local codes consider the magnetic shear, as well, by keeping the first order Taylor expansion of the safety factor profile in the $\rho^* \to 0$ limit – similar to the treatment of the background gradient terms in Eq. (11).

3.3. Spatial differentiation

Currently, both the radial (x) and the parallel (z) directions are discretized on a fixed equidistant grid, and finite difference schemes are applied for the numerical representation of derivatives. Typically, fourth-order centered schemes

turn out to be most efficient while providing reasonable accuracy. The third direction (y) is represented in Fourier space and thus allows for an exact representation of spatial derivatives. Alternatively, the nonlinear terms can be treated using a mixed spectral/finite difference variant of the Arakawa scheme [44]. The latter discretizes the nonlinear terms such that the conservation properties which are analytically fulfilled, are also retained numerically. With this scheme, the code achieves stable nonlinear saturation with small or even zero numerical dissipation in the perpendicular plane, allowing for more robust code operation than with standard centered differences. The implemented term is

$$\mathcal{N} = \frac{1}{3} \Big[\left(ik_y \bar{\xi}_1 \cdot \frac{\partial g_{1\sigma}}{\partial x} - \frac{\partial \bar{\xi}_1}{\partial x} \cdot ik_y g_{1\sigma} \right)$$
$$+ ik_y \left(\bar{\xi}_1 \cdot \frac{\partial g_{1\sigma}}{\partial x} - g_{1\sigma} \cdot \frac{\partial \bar{\xi}_1}{\partial x} \right)$$
$$+ \frac{\partial}{\partial x} \left(g_{1\sigma} \cdot ik_y \bar{\xi}_1 - \bar{\xi}_1 \cdot ik_y g_{1\sigma} \right) \Big], \quad (45)$$

where, for computational efficiency, all terms separated by dots ($\cdot$) are Fourier-transformed to real space before performing the multiplication.

3.4. Gyroaveraging

Several terms in the basic equations contain gyroaveraged quantities like

$$\bar{f}(\mathbf{x}) = \mathcal{G}\left[f(\mathbf{x})\right] = \frac{1}{2\pi} \oint d\theta\, f(\mathbf{x} + \mathbf{r}(\theta)) \quad (46)$$

where $\mathbf{r} = \mathbf{r}(\theta)$ is the (cyclic) gyroradius vector orthogonally aligned to the magnetic field and $\mathcal{G}$ denotes the aforementioned gyroaverage operator whose explicit representation is going to be derived in the following.

In a first step, periodic boundary conditions are utilized in the y direction which allows for switching to a Fourier representation. Hence, Eq. (46) can be written as

$$\bar{f}(\mathbf{x}) = \frac{1}{2\pi} \sum_{k_y} \int_0^{2\pi} d\theta\, f(x + r^x(\theta), k_y, z)\, e^{ik_y(y + r^y(\theta))} \quad (47)$$

12

where the contravariant components of $\mathbf{r}$ in the nonorthogonal flux tube coordinates is given by $r^x = \mathbf{r} \cdot \nabla x = \sqrt{g^{11}} \rho_\sigma \cos\theta$ and $r^y = \mathbf{r} \cdot \nabla y = \rho_\sigma (g^{12} \cos\theta + \sqrt{\gamma_1} \sin\theta)/\sqrt{g^{11}}$ if a linearized metric is considered. For the evaluation of the θ integration, interpolation techniques are obviously required. A finite elements approach seems to be a reasonable choice for this purpose. The function to be gyroaveraged is rewritten in terms of finite-element base functions $\Lambda_n(x)$ for each value of f on the coarse-grained grid at position $x_{(n)}$. Using the compact vector representation

$$f(x) = \mathbf{\Lambda}(x) \cdot \mathbf{f} \qquad (48)$$

with $\mathbf{\Lambda}(x) = (\Lambda_0(x), \ldots, \Lambda_{N_x-1}(x))^T$ and $\mathbf{f} = (f(x_{(0)}), \ldots, f(x_{(N_x-1)}))^T$ transforms Eq. (47) into

$$\bar{\mathbf{f}}(k_y, z, \mu) = \mathcal{G}(k_y, z, \mu) \cdot \mathbf{f}(k_y, z). \qquad (49)$$

The gyroaverage operator is thus a matrix with the elements

$$\mathcal{G}_{in}(k_y, z, \mu) = \frac{1}{2\pi} \int_0^{2\pi} \mathrm{d}\theta \Lambda_n(x_{(i)} + r^x) \, \mathrm{e}^{\mathrm{i}k_y r^y} \quad (50)$$

In order to avoid further computational effort, the base functions $\Lambda_n(x)$ are chosen such that the values on the coarse grid can easily be extracted again, which happens if the interpolated function coincides with the original values. Furthermore, $\Lambda_n(x)$ is considered to be finite just in the vicinity of the coarse grid point $x_{(n)}$, thus becoming zero when approaching the next neighboring grid point. Possible alternatives taking into account several grid points, for instance splines, would require a solution of a linear system of equations.

A simple choice in this context are polynomials of order p at each position $x_{(n)}$ following the boundary conditions

$$\left. \frac{\partial^u}{\partial x^u} P_{n,m}(x) \right|_{x=x_{(i)}} = \delta_{in}\delta_{um} \qquad (51)$$

for the mth derivative of the function which effectively amounts to a Hermite polynomial interpolation. Here, the indices are $i = n, (n+1)$ and $u = 0, \ldots, (p-1)/2$. Changing again to

a matrix-vector notation where $\mathbf{f}$ contains all function values on the coarse grid and $\mathbf{P}_m = (P_{0,m}, \ldots, P_{N_x-1,m})^T$, derivatives of mth order can be formally represented by the mth power of a matrix $\mathcal{D}$. The construction of the latter then depends on the finite difference scheme actually chosen for the numerical evaluation of derivatives which is a 4th order centered scheme. In summary, Eq. (48) becomes

$$f(x) = \mathbf{\Lambda}(x) \cdot \mathbf{f} = \sum_{m=0}^{(p-1)/2} \mathbf{P}_m(x) \mathcal{D}^m \mathbf{f}. \qquad (52)$$
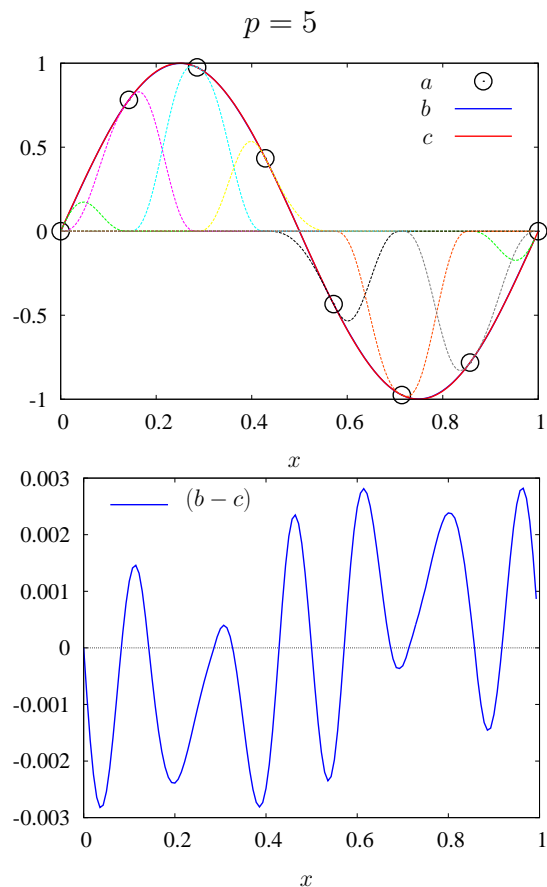
For most applications, polynomials of degree

Figure 3: Illustration and comparison of the finite element interpolation implemented in GENE . In the upper plot, black dots (a) represent the values of a test function $\sin(2\pi x)$ (c) on a coarse grid whereas the blue line (b) indicates interpolation results using the base functions drawn as dotted lines. Since differences between (b) and (c) are hardly visible, they are explicitly shown in the lower plot.

$p = 5$ as shown in Fig. 3 seem to be a good tradeoff between high accuracy and moderate computational effort.

13

3.5. Integration

Except for some post-processing applications, numerical integrations are almost exclusively performed in the velocity space since associated moments are required in the field equations. To allow for an optimum number of grid points, a Gaussian quadrature scheme with Gauß-Legendre weights and knots is used in the μ direction while the alternative extended Simpson's rule [45] is applied in the $v_\parallel$ direction.

4. Code verification

Some results obtained with the global GENE version are presented in this section and benchmarked against analytical and numerical test cases.

4.1. The local limit

A first obvious and important test is to check whether the global code eventually reaches the local limit with decreasing ρ^* parameter which is in the following given by $\rho^* = \rho_i/a$. As a side effect, judgments on the validity of local simulations for specific devices can be drawn. Naturally, the details of such a study depend to some extent on the chosen radial profiles which has been shown elsewhere [46, 15, 47]. In the present case, peaked temperature and density gradient profiles are chosen of the form

$$\hat{T}_{i,e} = \exp\left[-\kappa_T \varepsilon \Delta T \tanh\left(\frac{(x-x_0)/a}{\Delta T}\right)\right],$$

$$\hat{n}_{i,e} = \exp\left[-\kappa_n \varepsilon \Delta n \tanh\left(\frac{(x-x_0)/a}{\Delta n}\right)\right], \quad (53)$$

where $\kappa_T = \max(R_0/L_T) = 6.9589$ and $\kappa_n = \max(R_0/L_n) = 2.232$ denote the maximum gradient values, $\varepsilon = a/R_0 = 0.3616$ the inverse aspect ratio, and $\Delta T, \Delta n = 0.3$ the characteristical width of the gradient peak which is centered at $x_0 = 0.5\,a$. In addition, the flux surfaces are assumed to be circular and concentric with a safety factor profile of $q(x/a) = 0.498(x/a)^4 - 0.466(x/a)^3 + 2.373(x/a)^2 + 0.854$ such that $q_0 = q(x_0 = 0.5\,a) = 1.42$ matches the Cyclone Base Case (CBC) [48] value. Two species – electrons and one ion species – are considered with their mass ratio set to $m_i/m_e = 1836$ as in hydrogen plasmas. The resulting growth rates of linear simulations with a fixed binormal wavenumber of $k_y \rho_s \approx 0.284$ in the center of the simulation domain and a fixed reference β_{ref} value of 2.5% but varying ρ^* are shown in Fig. 4. The normalization used is the ion sound speed $c_s = \sqrt{T_e/m_i}$ divided by the tokamak major radius R_0. Obviously, the
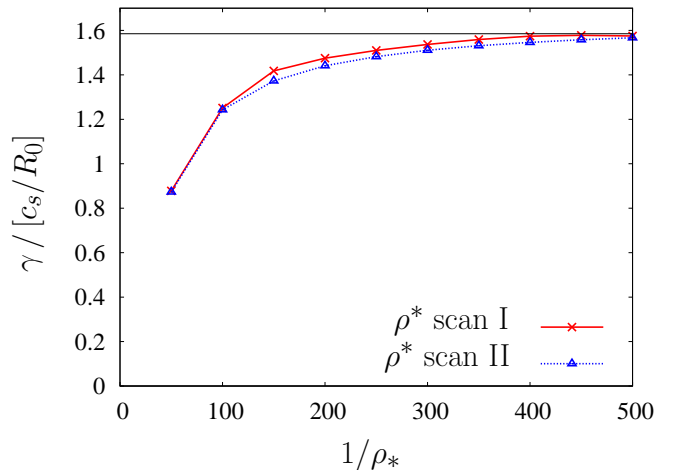

Figure 4: Growth rate at $k_y \rho_s \approx 0.284$ as function of the inverse ρ^* value. Here, kinetic electrons with a proton-electron mass ratio are considered as well as a finite β_{ref} of 2.5%. The temperature and density gradient profiles are peaked with $\Delta T_{i,e}, \Delta n = 0.3$. The radial simulation box is kept fixed with respect to (I) the gyroradius and (II) the minor radius. The local code result using the maximum gradients is shown as thin, black line.

local and global results converge for $\rho^* \lesssim 1/400$ – but even at $\rho^* \sim 1/200$, they differ only by less than 10%. This finding does not depend on the way the ρ^* scan is performed. As one option, the radial simulation box length can be kept fixed with respect to the gyroradius so that a smaller and smaller radial domain of the macroscopic profiles will be resolved with decreasing ρ^* (note that in this case, periodic boundary conditions have to be employed instead of Dirichlet boundary conditions else). Alternatively, the radial box size can be set to a fixed fraction of the minor radius, and hence the number of ion gyroradii within the domain is increasing with decreasing ρ^*. (In order to resolve those fine scales, more and more radial grid points need to be employed, making this second approach computationally much more chal-

lenging.) The first approach has been chosen for another set of linear investigations where β has been modified. The resulting growth rates of the
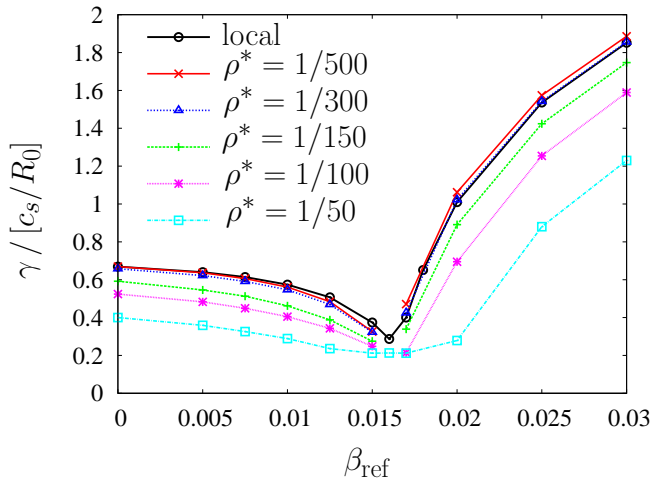

Figure 5: Growth rate at $k_y \rho_s \approx 0.284$ as function of the β_{ref} for different values of ρ^* together with the local code result. The global growth rates resemble the local ones but are reduced in amplitude depending on the gyroradius-to-machine-size ratio

corresponding ITG-KBM transition are presented in Fig. 5 for several values of ρ^*. Generally, the variation of the global growth rates qualitatively resembles the local one but is reduced in amplitude depending on the gyroradius-to-machine-size ratio.

These local limit tests can be considered successful, serving as a first indicator for the reliability of the global-GENE implementation. However, comparisons with analytical models or other codes allow for a more comprehensive evaluation and will thus be presented in the following sections.

4.2. Rosenbluth-Hinton test

A well established test for gyrokinetic codes is based on the time evolution of an initial $\mathbf{E} \times \mathbf{B}$ zonal flow impulse in a toroidal plasma with circular flux surfaces and a large aspect ratio. In the absence of collisions and any nonlinear coupling, a rapid but damped oscillation of the geodesic acoustic mode (GAM) [49] is observed which re-

laxes to a finite stationary value A_R so that

$$\frac{\langle \phi_1 \rangle_{\mathrm{FS}}(x, t)}{\langle \phi_1 \rangle_{\mathrm{FS}}(x, t = 0)} = (1 - A_R)\, \mathrm{e}^{-\gamma_G t} \cos(\omega_G t) + A_R. \tag{54}$$

In the local limit – i.e., neglecting radial couplings – and for adiabatic electrons, the residual has been analytically predicted by Rosenbluth and Hinton [50, 51] to be

$$A_R = \frac{1}{1 + 1.6\, q(r)^2 / \sqrt{r/R_0}}. \tag{55}$$

Since zonal flows are identified as one of the most important saturation mechanisms in several parameter regimes, for instance in ITG mode dominated turbulence, it is widely accepted that this test has to be passed by gyrokinetic codes.

In the following investigation, the same safety factor profile as before is employed but temperature and density profiles are taken to be constant as in the analytic calculation. The number of grid points in the $(x, z, v_\parallel, \mu)$ directions is $(63 \times 16 \times 128 \times 16)$ and the box lengths are chosen to be $(L_x, L_{v_\parallel}, L_\mu) = (48\rho_{\mathrm{ref}}, 3\, v_{Ti}(x_0), 9\, T_{0i}(x_0)/B_{\mathrm{ref}})$. The resulting residual levels at the center of the simulation domain are plotted in Fig. 6 for several values of ρ^*. While the deviation from
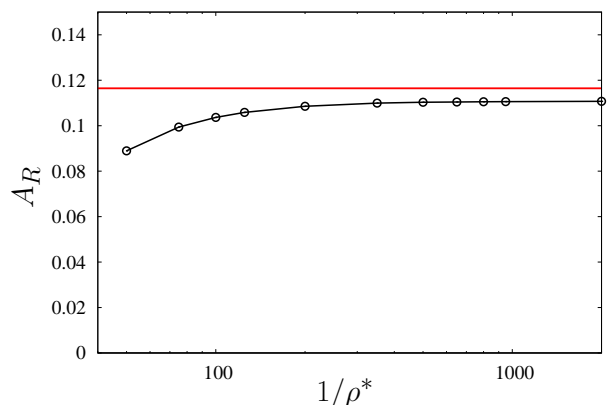

Figure 6: Rosenbluth-Hinton residual (black dots and line) evaluated at the radial center position of the simulation box for different settings of ρ^*. The red line indicates the Rosenbluth-Hinton prediction.

the Rosenbluth-Hinton prediction is significant at large ρ^*, it becomes less than 10% at $1/\rho^* \gtrsim 200$

and thus demonstrates a reasonably good agreement when taking into account the relatively large inverse aspect ratio and effective $k_x^{\min}$ mode.

A further example employs parameters being similar but not identical to those presented in Ref. [21]. In particular, they prescribe a linear safety factor profile $q(x/a) = 0.7 + 0.9 \cdot (x/a)$ and an inverse aspect ratio of $a/R_0 = 1/10$. With this choice, an even better agreement with the analytic prediction can be expected, although ρ^* is taken to be $1/40$. The numerical parameters are the same as before, except for the radial direction where 48 grid points are taken along a box length of $L_x = 38\rho_{\mathrm{ref}}$. Contrary to local codes where exactly one safety factor q and radial position x/R_0 are chosen and thus just one residual can be investigated per simulation, a global code automatically provides results for a wide parameter range. Hence, the residual levels and oscillation frequencies gained by fitting are displayed for all radial positions except for the two outermost grid points in Fig. 7. The analytical results, given by Eq. (55) and

$$\omega_G \frac{R_0}{c_s} = \sqrt{\frac{(7/\tau_e + 4)\mathcal{A}_G}{2}} \qquad (56)$$

with $\tau_e = T_e/T_i$ and $\mathcal{A}_G = [1 + (2(23 + 16\tau_e + 4\tau_e^2))/(q(7 + 4\tau_e))^2]$ [52], are included for comparison. Clearly, both values agree well with the predictions within $0.3 \lesssim x/a \lesssim 0.8$. The deviations at the remaining radial positions can be attributed to the Dirichlet boundary condition. Considering the relatively large reference gyroradius $\rho_s = 0.025\,a$ employed in this simulation, it is obvious that gyroaverages at intermediate to high μ values, which might partially be calculated outside the simulation domain, may exhibit an influence even at radial positions being far away from the boundaries. Indeed, simulations at smaller ρ^* ($\rho^* = 1/100, 1/200$), possess a narrower transition region but do not show such excellent agreement. For instance, numerical and analytical residual levels deviate up to about 20% at $x/a = 0.3$. Hence, the remarkable coincidence found in the present case seems to be restricted to a very narrow parameter regime.
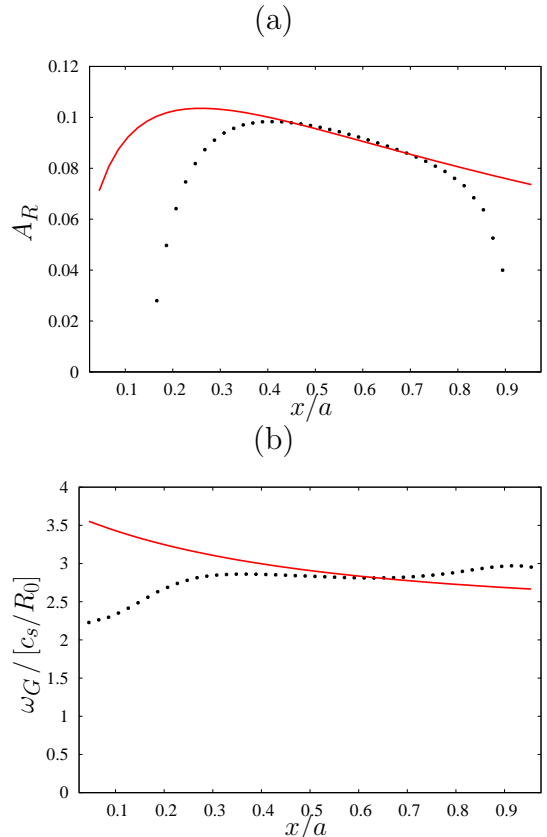

Figure 7: Rosenbluth-Hinton residual (a) and oscillation frequency (b) evaluated at all radial positions except for the two outermost grid points. The black dots represent numerical results whereas the red solid line illustrates the analytical prediction. Note that (unphysical) negative values of A_R are suppressed close to the boundaries.

4.3. Linear benchmark

Having successfully passed the Rosenbluth-Hinton and local limit tests, more complicated scenarios involving more comprehensive physical effects can be studied.

In this section, direct comparisons between GENE and the global particle-in-cell (PIC) code GYGLES [53] solving the linear gyrokinetic equations are presented. Once again, parameters similar to the CBC set are employed so that $\varepsilon = a/R_0 = 0.6043\,\mathrm{m}/1.6714\,\mathrm{m} = 0.3616$. The temperature and density profiles of the gyrokinetic ions and adiabatic electrons are assumed to follow Eq. (53) with gradient peak values of $\kappa_T = 6.9589$ and $\kappa_n = 2.2320$ at $x_0 = 0.5\,a$. The characteristical widths are set to $\Delta T = \Delta n = 0.3$. Extracting from the DIII-D discharge 81499 which constitutes the CBC basis, a temperature

of $T_0(x_0) = 1.9693\,\text{keV}$ and a reference magnetic field of $B_{\text{ref}} = 1.9\,\text{T}$ allows for estimating $\rho^* \approx 1/180$ in case of pure deuterium plasmas. The geometry is chosen to be circular concentric as before with a parabolic safety factor profile of

$$q(x/a) = 0.854 + 2.4045\,(x/a)^2. \qquad (57)$$

The resulting growth rates and frequencies obtained by GYGLES [54] and GENE using Dirichlet boundary conditions are presented in Fig. 8 and show excellent agreement except for the highest k_y modes. However, this deviation can be explained
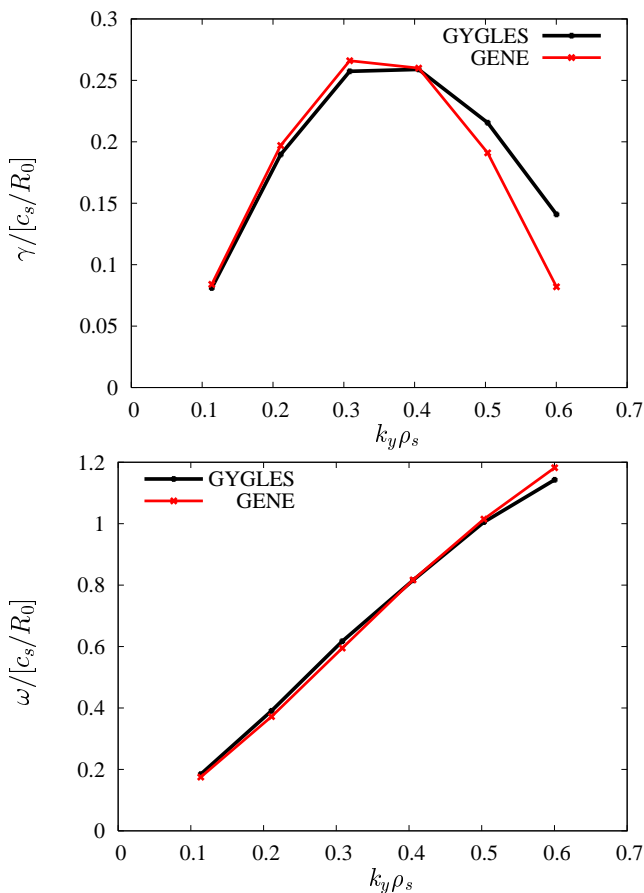
Figure 8: A comparison of growth rates (left) and real frequencies (right) calculated by the linear, gyrokinetic PIC code GYGLES and the global GENE version for an adiabatic electron test case further described in the text.

by the different treatment of gyroaverage and field operators at these wave numbers. In the GYGLES version at hand, a long wavelength approximation, $k_\perp\rho \ll 1$, is applied so that Larmor radius effects are kept up to second order $(k_\perp\rho)^2$ while all orders are considered in GENE.

The numerical GENE parameters employed in the present linear study are the following. At each binormal wave number, the radial box size is set to $L_x = 160\rho_s$ and 16 grid points are used in the parallel direction. All remaining grid sizes and resolutions vary. For instance, at low wave numbers, i.e. $k_y\rho_s < 0.5$, $(160{\times}32{\times}16)$ grid points in the $(x, v_\parallel, \mu)$ directions and a velocity space box of $(L_{v_\parallel}, L_\mu) = (3\,v_{Ti}(x_0), 9\,T_{0i}(x_0)/B_{\text{ref}})$ turn out to be sufficient while at higher wave numbers up to $(256 \times 64 \times 128)$ grid points and $(L_{v_\parallel}, L_\mu) = (5\,v_{Ti}(x_0), 18\,T_{0i}(x_0)/B_{\text{ref}})$ are required.

4.4. Nonlinear benchmark

In 2008, a test case for nonlinear gyrokinetic simulations with adiabatic electrons has been defined within the framework of the European Integrated Tokamak Modeling (ITM) benchmarking effort [55] and was considered to check the nonlinear GENE behavior.

The underlying physical parameters are very similar to those used in the linear GYGLES-GENE comparison so that only important deviations are listed in the following. In particular, they comprise the temperature and density profiles since their gradients are not peaked but flat over a wide radial range,

$$\omega_{(T,n)}(r) = \kappa_{(T,n)}\left(1 - \text{sech}^2\left[(r - r_i)/(a\Delta r)\right] - \text{sech}^2\left[(r - r_a)/(a\Delta r)\right]\right) \qquad (58)$$

with $r_i/a = 0.1$, $r_a/a = 0.9$ and $\Delta r = 0.04$.

The benchmark itself describes a nonlinear relaxation problem, i.e. no additional sources or sinks are applied. The chosen observable is the volume averaged turbulent, ion thermal diffusivity as a function of the average ion temperature gradient, both averages done over the radial domain $0.4 < r/a < 0.6$. Sampling both values at successive time points generates a *cloud* of points as can be seen in Fig. 9. The following stages can be identified: At the beginning, the thermal diffusivity grows at a fixed temperature gradient, thus clearly reflecting the linear phase. As soon as the nonlinearity becomes important, an overshoot occurs which is followed by a first saturation phase where the diffusivity and the gradient both
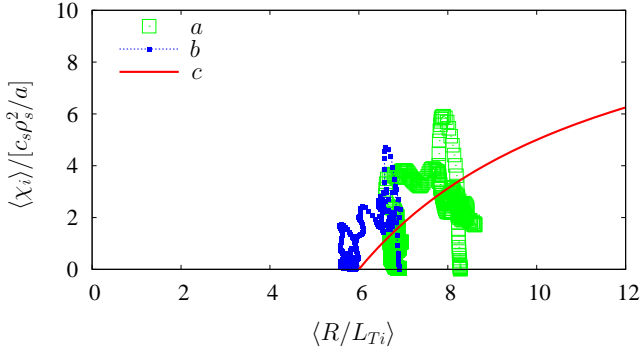
Figure 9: Volume averaged turbulent ion thermal diffusivity in units of $\chi_{\mathrm{GB}} = c_s\rho_s^2/a$ vs. the normalized ion temperature gradient. The points represent both values at successive time points. Here, nonlinear GENE simulation results are shown for two different initial gradient settings (a) and (b), together with the reference result obtained from local simulations [48] (c).

fluctuate around a constant value for some time. Eventually, the ion temperature profile starts to relax and thus lowers the heat diffusivity. All these features have been found within the ITM benchmarking effort by the nonlinear, gyrokinetic PIC codes ORB5, GYSELA [29, 56], and ELM-FIRE [57]. A comparison of Fig. 9 with Fig. 2 in Ref. [55] confirms that the GENE results using Dirichlet boundary conditions well fit with those of the ITM benchmark.

For a very extensive nonlinear benchmark between ORB5 and GENE using heat sources and sinks in order to allow for a quasi-stationary state comparison, the reader is furthermore referred to Ref. [22].

4.5. Code performance and parallelization

In order to perform time efficient computations and to treat large problem sizes, massive parallelization is called for. For instance, the grid resolution for a typical two-species, nonlocal and nonlinear trapped electron mode turbulence simulation for a medium-sized tokamak can be estimated to $512 \times 32 \times 24 \times 64 \times 24$ in the $x, k_y, z, v_\parallel, \mu$ directions which roughly translates to $200\,\mathrm{GB}$ memory. In terms of computational time, several $100\,\mathrm{kCPUh}$ can be expected. GENE thus offers MPI parallelization along all of the $(x, y, z, v_\parallel, \mu)$ directions as well as over the species label, and it also provides the possibility to use OpenMP.

Hence, the code is able to run on several 10,000 cores. However, determining the most efficient MPI mapping then clearly constitutes a nontrivial task which is why GENE is equipped with an automatic detection comparing the timings of all available mappings during initialization. Furthermore, an effort has been made to automatically adapt the code to the available cache size which typically varies from machine to machine. For this purpose, two or more alternatives are implemented for core parts of GENE which differ in the way the arrays are distributed in memory and which are also compared with respect to the runtime during initialization. In extreme cases, a factor of 10 has been saved compared to a single implementation being used on all available architectures. Examples of GENE scalings using the local approximation can, e.g., be found in Ref. [10]. A strong scaling, i.e. increasing the number of cores while keeping the system size constant, computed on the EPCC Hector CRAY XE6 machine for the global parameters described above is additionally shown in Fig. 10.
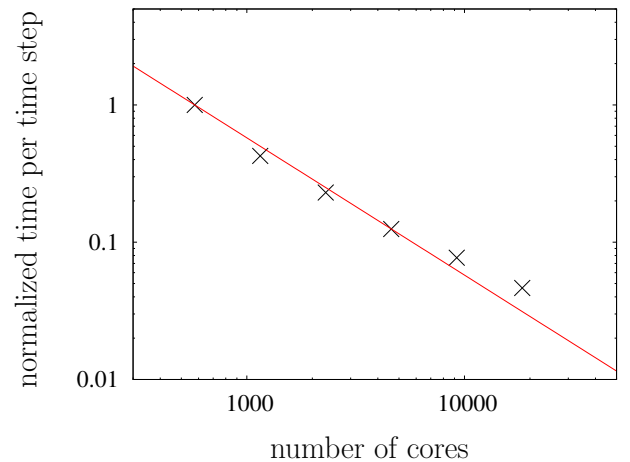

Figure 10: Strong scaling, i.e. time per time step normalized to its value at 576 cores as a function of the number of cores for global computations on the EPCC Hector CRAY XE6 machine with respective resolutions $n_x \times n_{ky} \times n_z \times n_{v_\parallel} \times n_\mu \times n_{spec} = 512 \times 32 \times 24 \times 64 \times 24 \times 2$.

18

5. Conclusions

The grid-based gyrokinetic turbulence code GENE has been extended to include radial variations of the background profiles and metric coefficients, thus enabling investigations of nonlocal phenomena. In addition, various types of source/sink terms have been added which allow for a control of the profile evolution. The numerical implementation of the underlying equation has been discussed and several verification studies have been presented which confirm the maturity and correctness of the software. Finally, a good parallel performance has been demonstrated which is an essential prerequisite due to the enormous computational effort being required to resolve the turbulent structures while considering a large radial fraction of a fusion device.

[1] A. J. Brizard, T. S. Hahm, Foundations of nonlinear gyrokinetic theory, Rev. Mod. Phys. 79 (2007) 421.

[2] X. Garbet, Y. Idomura, L. Villard, T. H. Watanabe, TOPICAL REVIEW: Gyrokinetic simulations of turbulent transport, Nucl. Fusion 50 (2010) 043002.

[3] F. Jenko, The GENE development team, The GENE code (Mar 2011).
URL http://gene.rzg.mpg.de

[4] F. Jenko, W. Dorland, M. Kotschenreuther, B. N. Rogers, Electron temperature gradient driven turbulence, Phys. Plasmas 7 (2000) 1904–1910.

[5] T. Dannert, F. Jenko, Gyrokinetic simulation of collisionless trapped-electron mode turbulence, Phys. Plasmas 12 (2005) 072309.

[6] T. Dannert, Gyrokinetische Simulation von Plasmaturbulenz mit gefangenen Teilchen und elektromagnetischen Effekten, Ph.D. thesis, Technische Universität München (2005).

[7] H. Lederer, R. Hatzky, R. Tisma, A. Bottino, F. Jenko, Hyperscaling of plasma turbulence simulations in deisa, in: CLADE '07: Proceedings of the 5th IEEE workshop on Challenges of large applications in distributed environments, ACM, New York, NY, USA, 2007, pp. 19–26.

[8] F. Merz, Gyrokinetic simulation of multimode plasma turbulence, Ph.D. thesis, Westfälische Wilhelms-Universität Münster (2008).

[9] M. J. Pueschel, Electromagnetic effects in gyrokinetic simulations of plasma turbulence, Ph.D. thesis, Westfälische Wilhelms-Universität Münster (2009).

[10] H. Lederer, R. Tisma, R. Hatzky, A. Bottino, F. Jenko, Petascaling of plasma turbulence codes, parallel computing: Architectures , algorithms and applications, Advances in Parallel Computing 15 (2008) 713.

[11] Y. Sarazin, X. Garbet, P. Ghendrih, S. Benkadda, Transport due to front propagation in tokamaks, Phys. Plasmas 7 (2000) 1085–1088.

[12] J. Candy, R. E. Waltz, An Eulerian gyrokinetic-Maxwell solver, J. Comput. Phys. 186 (2003) 545–581.

[13] B. F. McMillan, S. Jolliet, T. M. Tran, L. Villard, A. Bottino, P. Angelino, Avalanchelike bursts in global gyrokinetic simulations, Phys. Plasmas 16 (2009) 022310.

[14] G. Dif-Pradalier, P. H. Diamond, V. Grandgirard, Y. Sarazin, J. Abiteboul, X. Garbet, P. Ghendrih, A. Strugarek, S. Ku, C. S. Chang, On the validity of the local diffusive paradigm in turbulent plasma transport, Phys. Rev. E 82 (2010) 025401–+. doi:10.1103/PhysRevE.82.025401.

[15] T. Görler, Multiscale effects in plasma microturbulence, Ph.D. thesis, Universität Ulm (2009).

[16] X. Lapillonne, Microturbulence in electron internal transport barriers in the tcv tokamak and global effects, Ph.D. thesis, École Polytechnique Fédérale de Lausanne (2010).

[17] J. Candy, R. E. Waltz, S. E. Parker, Y. Chen, Relevance of the parallel nonlinearity in gyrokinetic simulations of tokamak plasmas, Phys. Plasmas 13 (2006) 074501.

[18] Y. Idomura, M. Ida, S. Tokuda, L. Villard, New conservative gyrokinetic full-f Vlasov code and its comparison to gyrokinetic δf particle-in-cell code, J. Comput. Phys. 226 (2007) 244–262.

[19] S. Jolliet, Gyrokinetic particle-in-cell global simulations of ion-temperature-gradient and collisionless-trapped-electron-mode turbulence in tokamaks, phd thesis no. 4326, Ph.D. thesis, Ecole Polytechnique Fédérale de Lausanne (2009).

[20] X. Lapillonne, S. Brunner, T. Dannert, S. Jolliet, A. Marinoni, L. Villard, T. Görler, F. Jenko, F. Merz, Clarifications to the limitations of the s-alpha equilibrium model for gyrokinetic computations of turbulence, Phys. Plasmas 16 (2009) 032308.

[21] S. Jolliet, A. Bottino, P. Angelino, R. Hatzky, T. Tran, B. McMillan, O. Sauter, K. Appert, Y. Idomura, L. Villard, A global collisionless PIC code in magnetic coordinates, Comput. Phys. Commun. 177 (2007) 409–425.

[22] X. Lapillonne, B. F. McMillan, T. Görler, S. Brunner, T. Dannert, F. Jenko, F. Merz, L. Villard, Nonlinear quasisteady state benchmark of global gyrokinetic codes, Phys. Plasmas 17 (2010) 112321.

[23] R. G. Littlejohn, Hamiltonian formulation of guiding center motion, Phys. Fluids 24 (1981) 1730–1749.

[24] W. D. D'haeseleer, W. N. G. Hitchon, J. D. Callen, J. L. Shohet, Flux Coordinates and Magnetic Field Structure. A Guide to a Fundamental Tool of Plasma Theory, Springer-Verlag, New York, 1991.

[25] J. C. Cummings, Gyrokinetic simulation of finite-beta and self-generated sheared-flow effects on pressure-gradient-driven instabilities, Ph.D. thesis, Princeton University, Princeton (1995).

[26] J. D. Huba, NRL (Naval Research Laboratory) plasma formulary (2007).

[27] B. F. McMillan, S. Jolliet, T. M. Tran, L. Villard, A. Bottino, P. Angelino, Long global gyrokinetic simulations: Source terms and particle noise control, Phys. Plasmas 15 (2008) 052308.

[28] Y. Sarazin, V. Grandgirard, J. Abiteboul, S. Allfrey, X. Garbet, P. Ghendrih, G. Latu, A. Strugarek, G. Dif-Pradalier, Large scale dynamics in flux driven gyrokinetic turbulence, Nucl. Fusion 50 (2010) 054004.

[29] V. Grandgirard, Y. Sarazin, P. Angelino, A. Bottino, N. Crouseilles, G. Darmet, G. Dif-Pradalier, X. Garbet, P. Ghendrih, S. Jolliet, G. Latu, E. Sonnendrücker, L. Villard, Global full-f gyrokinetic simulations of plasma turbulence, Plasma Phys. Control. Fusion 49 (2007) B173.

[30] V. Shafranov, in: Reviews of Plasma Physics, M.A. Leontovich, Consultants Bureau, New York, Vol. 1, p. 1, 1966.

[31] H. Lütjens, A. Bondeson, O. Sauter, Comput. Phys. Comm. 97 (1996) 219.

[32] P. Xanthopoulos, F. Jenko, Clebsch-type coordinates for nonlinear gyrokinetics in generic toroidal configurations, Phys. Plasmas 13 (2006) 092301.

[33] W. E. Schiesser, The Numerical Method of Lines: Integration of Partial Differential Equations, Academic Press, New York, 1991.

[34] V. Hernandez, J. E. Roman, V. Vidal, SLEPc: A scalable and flexible toolkit for the solution of eigenvalue problems, ACM Transactions on Mathematical Software 31 (2005) 351–362.

[35] V. Hernandez, J. E. Roman, E. Romero, A. Tomas, V. Vidal, SLEPc home page, http://www.grycap.upv.es/slepc (2009).

[36] S. Balay, K. Buschelman, W. D. Gropp, D. Kaushik, M. G. Knepley, L. C. McInnes, B. F. Smith, H. Zhang, PETSc Web page, http://www.mcs.anl.gov/petsc (2001).

[37] S. Balay, K. Buschelman, V. Eijkhout, W. D. Gropp, D. Kaushik, M. G. Knepley, L. C. McInnes, B. F. Smith, H. Zhang, PETSc users manual, Tech. Rep. ANL-95/11 - Revision 2.1.5, Argonne National Laboratory (2004).

[38] S. Balay, W. D. Gropp, L. C. McInnes, B. F. Smith, Efficient management of parallelism in object oriented numerical software libraries, in: E. Arge, A. M. Bruaset, H. P. Langtangen (Eds.), Modern Software Tools in Scientific Computing, Birkhäuser Press, 1997, pp. 163–202.

[39] J. L. Mead, R. A. Renaut, Optimal Runge-Kutta Methods for First Order Pseudospectral Operators, J. Comput. Phys. 152 (1999) 404–419.

[40] K. V. Roberts, J. B. Taylor, Gravitational Resistive Instability of an Incompressible Plasma in a Sheared Magnetic Field, Phys. Fluids 8 (1965) 315–322.

[41] S. C. Cowley, R. M. Kulsrud, R. Sudan, Considerations of ion-temperature-gradient-driven turbulence, Phys. Fluids B 3 (1991) 2767–2782.

[42] M. A. Beer, S. C. Cowley, G. W. Hammett, Field-aligned coordinates for nonlinear simulations of tokamak turbulence, Phys. Plasmas 2 (1995) 2687–2700.

[43] B. Scott, Global consistency for thin flux tube treatments of toroidal geometry, Phys. Plasmas 5 (1998) 2334–2339.

[44] A. Arakawa, Computational design for long-term numerical integration of the equations of fluid motion: Two-dimensional incompressible flow. Part I, J. Comput. Phys. 1 (1966) 119 – 143.

[45] W. H. Press, B. P. Flannery, W. T. Vetterling, S. A. Teukolsky, Numerical Recipes in Pascal: The Art of Scientific Computing, Cambridge University Press, Cambridge, 1989.

[46] J. Candy, R. E. Waltz, W. Dorland, The local limit of global gyrokinetic simulations, Phys. Plasmas 11 (2004) L25–L28.

[47] L. Villard, A. Bottino, S. Brunner, A. Casati, J. Chowdhury, T. Dannert, R. Ganesh, X. Garbet, T. Görler, V. Grandgirard, R. Hatzky, Y. Idomura, F. Jenko, S. Jolliet, S. Khosh Aghdam, X. Lapillonne, G. Latu, B. F. McMillan, F. Merz, Y. Sarazin, T. M. Tran, T. Vernay, Gyrokinetic simulations of turbulent transport: size scaling and chaotic behaviour, Plasma Phys. Controlled Fusion 52 (2010) 124038.

[48] A. M. Dimits, G. Bateman, M. A. Beer, B. I. Cohen, W. Dorland, G. W. Hammett, C. Kim, J. E. Kinsey, M. Kotschenreuther, A. H. Kritz, L. L. Lao, J. Mandrekas, W. M. Nevins, S. E. Parker, A. J. Redd, D. E. Shumaker, R. Sydora, J. Weiland, Comparisons and physics basis of tokamak transport models and turbulence simulations, Phys. Plasmas 7 (2000) 969–983.

[49] N. Winsor, J. L. Johnson, J. M. Dawson, Geodesic Acoustic Waves in Hydromagnetic Systems, Phys. Fluids 11 (1968) 2448–2450.

[50] M. N. Rosenbluth, F. L. Hinton, Poloidal Flow Driven by Ion-Temperature-Gradient Turbulence in Tokamaks, Phys. Rev. Lett. 80 (1998) 724–727.

[51] F. L. Hinton, M. N. Rosenbluth, Dynamics of axisymmetric and poloidal flows in tokamaks , Plasma Phys. Control. Fusion 41 (1999) A653–A662.

[52] H. Sugama, T.-H. Watanabe, Collisionless damping of geodesic acoustic modes, J. Plasma Phys. 72 (2006) 825.

[53] M. Fivaz, S. Brunner, G. de Ridder, O. Sauter,

T. M. Tran, J. Vaclavik, L. Villard, K. Appert, Finite element approach to global gyrokinetic Particle-In-Cell simulations using magnetic coordinates, Comput. Phys. Commun. 111 (1998) 27–47.

[54] L. Villard, private communication (2009).

[55] G. L. Falchetto, B. D. Scott, P. Angelino, A. Bottino, T. Dannert, V. Grandgirard, S. Janhunen, F. Jenko, S. Jolliet, A. Kendl, B. F. McMillan, V. Naulin, A. H. Nielsen, M. Ottaviani, A. G. Peeters, M. J. Pueschel, D. Reiser, T. T. Ribeiro, M. Romanelli, The European turbulence code benchmarking effort: turbulence driven by thermal gradients in magnetically confined plasmas, Plasma Phys. Control. Fusion 50 (2008) 124015.

[56] V. Grandgirard, Y. Sarazin, X. Garbet, G. Dif-Pradalier, P. Ghendrih, N. Crouseilles, G. Latu, E. Sonnendrücker, N. Besse, P. Bertrand, Computing ITG turbulence with a full-f semi-Lagrangian code, Commun. Nonlinear Sci. Numer. Simul. 13 (2008) 81–87.

[57] J. A. Heikkinen, S. J. Janhunen, T. P. Kiviniemi, F. Ogando, Full f gyrokinetic method for particle simulation of tokamak transport, J. Comput. Phys. 227 (2008) 5582–5609.